Journal Pre-proofs

Mitoxantrone-loaded lipid nanoparticles for breast cancer therapy – quality-by-design approach and efficacy assessment in 2D and 3D *in vitro* cancer models

Andreia Granja, Rita Lima-Sousa, Cátia G. Alves, Duarte de Melo-Diogo, Marina Pinheiro, Célia T. Sousa, Ilídio J. Correia, Salette Reis

PII: S0378-5173(21)00850-4
DOI: https://doi.org/10.1016/j.ijpharm.2021.121044
Reference: IJP 121044

To appear in: *International Journal of Pharmaceutics*

Received Date: 18 June 2021
Revised Date: 4 August 2021
Accepted Date: 21 August 2021

Please cite this article as: A. Granja, R. Lima-Sousa, C.G. Alves, D. de Melo-Diogo, M. Pinheiro, C.T. Sousa, I.J. Correia, S. Reis, Mitoxantrone-loaded lipid nanoparticles for breast cancer therapy – quality-by-design approach and efficacy assessment in 2D and 3D *in vitro* cancer models, *International Journal of Pharmaceutics* (2021), doi: https://doi.org/10.1016/j.ijpharm.2021.121044

Mitoxantrone-loaded lipid nanoparticles for breast cancer therapy – quality-by-design approach and efficacy assessment in 2D and 3D *in vitro* cancer models.

Andreia Granja[a], Rita Lima-Sousa[b], Cátia G. Alves[b], Duarte de Melo-Diogo[b], Marina Pinheiro[a], Célia T. Sousa[c], Ilídio J. Correia[b,d,*] and Salette Reis[a,*]

[a]LAQV, REQUIMTE, Departamento de Ciências Químicas, Faculdade de Farmácia, Universidade do Porto, 4050-313 Porto, Portugal

[b]CICS-UBI – Centro de Investigação em Ciências da Saúde, Universidade da Beira Interior, 6200-506 Covilhã, Portugal

[c]IFIMUP and Departamento de Física e Astronomia da Faculdade de Ciências da Universidade do Porto, Rua do Campo Alegre 687, 4169-007, Porto, Portugal

[d]CIEPQPF – Departamento de Engenharia Química, Universidade de Coimbra, Rua Sílvio Lima, 3030-790 Coimbra, Portugal

*Corresponding authors: Ilídio J. Correia: icorreia@ubi.pt; Salette Reis: shreis@ff.up.pt;

Abstract

Breast cancer is the leading cause of cancer-related deaths among women worldwide. The conventional chemotherapeutic regimens used in the treatment of this disease often lead to severe side-effects and reduced efficacy. In this study, a novel drug delivery system for the chemotherapeutic drug mitoxantrone (Mito) was developed using solid lipid nanoparticles (SLN). The production of the SLN was carried out using an organic-solvent-free, low-cost method and optimized using a Box-Behnken design. SLN presented adequate size for cancer-related applications, more than 90% of EE% and remained stable for at least 6 months. A much higher drug release was obtained at acidic pH (mimicking the endosomal compartment) than plasmatic pH, highlighting the potential of the nanosystem for tumor drug delivery. Additionally, SLN were non-hemolytic and cytocompatible, even at high concentrations of lipid. A significantly higher anti-cancer efficacy was obtained for Mito-loaded SLN comparing to the free drug at different concentrations in MCF-7 2D models. Finally, the nanoformulation was evaluated in heterotypic breast cancer spheroids showing capacity to penetrate the tridimensional structure and ability to induce a high anti-tumoral effect, similarly to the free drug. Overall, these results support that the developed SLN are effective Mito nanocarriers for the treatment of breast cancer.

Keywords: Solid lipid nanoparticles (SLN), Mitoxantrone, Box-Behnken design, Chemotherapy, Breast cancer, Tumor spheroids.

1. Introduction

Breast cancer is the most commonly diagnosed cancer and the leading cause of cancer deaths in women worldwide, with more than 2.2 million new cases and approximately 685,000 deaths reported in 2020 (Sung et al., 2021). The costs associated with this disease are also a matter of concern. In 2009 breast cancer accounted for the second highest total economic costs among all cancers in Europe (€15 billion) and the highest healthcare costs (€6.73 billion) (Luengo-Fernandez et al., 2013). Those rise substantially as the disease progresses, with the healthcare costs of distant breast cancer increasing by 165% compared to local disease (Sun et al., 2018). The conventional treatment for this pathology includes local therapy to remove the tumor and adjacent tissues and adjuvant systemic therapies, such as chemotherapy, hormonal, and targeted therapies. Most of the drugs currently used, however, have a reduced cancer-cell specificity, along with poor pharmacological properties (Mei et al., 2013; Minchinton and Tannock, 2006). This requires administration of higher dosages leading to systemic toxicity and the occurrence of several adverse side-effects with different degrees of severity. These toxic effects compromise the maximum tolerated doses and the efficacy of the drugs (Blanco and Ferrari, 2014). Moreover, cancer cells may develop multidrug resistance, which results in lower responses to treatment and favors metastasis and disease recurrence (Bai et al., 2018). Mitoxantrone (Mito) is a synthetic anticancer agent from the class of anthracenediones with demonstrated efficacy in treating different malignancies such as acute leukemia, lymphomas, melanoma, and advanced breast cancer (Posner et al., 1985; Rossato et al., 2013; Varadwaj et al., 2010). However, as in most chemotherapeutic drugs, its cell killing effect is not cancer cell-specific, causing diverse side-effects, namely cardiotoxicity and myelosuppression (Posner et al., 1985; Rossato et al., 2013; Varadwaj et al., 2010).

Nanotechnology can have an important contribution in increasing the therapeutic index of chemotherapeutic drugs and developing safer and more effective treatment modalities (Wicki et al., 2015). Different Mito nanodelivery vehicles for breast cancer therapy have been reported in the literature, including liposomes (Mei et al., 2020; Pedrosa et al., 2015), mesoporous silica (Ma et al., 2011), magnetic (Sargazi et al., 2018) and gold (Imanparast et al., 2018) nanoparticles. In particular, lipid nanoparticles, such as solid lipid nanoparticles (SLN) are biodegradable, biocompatible (composed by lipids with generally recognized as safe (GRAS) status) and versatile types of nanocarriers, which makes them attractive for cancer therapy applications (Lasa-Saracibar et al., 2012). Compared to other Mito nanocarriers, such as liposomes, currently under clinical trials (Wang et al., 2020), lipid nanoparticles have several benefits such as high physical stability, the possibility of using cost-effective and green production methods, and easy large-scale production, which highlights their potential for translation into clinics (Feng and Mumper, 2013). A few studies have

reported the use of SLN as delivery vehicles of mitoxantrone for breast cancer therapy (Lu et al., 2006; Zhuang et al., 2012). To the best of our knowledge, however, the production of Mito-loaded SLN from green methods has not been reported yet. In addition, the evaluation of the anti-cancer efficacy Mito-loaded SLN in heterotypic breast cancer tumor spheroids has also not been described.

The aim of this work is to develop an affordable and effective Mito delivery system to improve breast cancer therapy and reduce the systemic toxic effects induced by the free drug. SLN were produced using an organic solvent-free, low-cost method. A Box-Behnken design was implemented for a cost-effective and rational optimization of the nanoformulation (Lawrence et al., 2014; Mishra et al., 2018). Detailed characterization was then conducted, the release profile of the drug at physiological and acidic pH was assessed, and the hemocompatibility and cytocompatibility were evaluated. Finally, the efficacy of the nanoformulation was determined in 2D and 3D *in vitro* breast cancer cell models.

2. Materials and Methods

2.1. Materials

Mitoxantrone hydrochloride, Tween® 80, Triton™ X-100 (TX-100), Sodium acetate, Phosphate Buffered Saline (PBS), Dulbecco's modified Eagle's medium F-12 (DMEM-F12), penicillin/streptomycin, trypsin, resazurin and paraformaldehyde were acquired from Sigma-Aldrich® (Sintra, Portugal). Roswell Park Memorial Institute (RPMI-1640) medium was purchased from Gibco (Invitrogen Corporation, Paisley, UK). Cetyl Palmitate was kindly offered by Gatefossé (Nanterre, France). Acetic acid glacial was obtained from VWR International LLC (Radnor PA, USA). Sodium chloride was purchased from Honeywell Fluka™ (NJ, USA). Fetal Bovine Serum (FBS) was purchased from Biochrom AG (Berlin, Germany). Calcein-AM, Propidium Iodide (PI), cell culture plates and T-flasks were purchased from Thermo Fisher Scientific (Porto, Portugal). Agarose was obtained from Grisp (Porto, Portugal). Michigan Cancer Foundation-7 (MCF-7) cell line was acquired from ATCC (Middlesex, UK). Normal Human Dermal Fibroblasts (NHDF) were purchased from Promocell (Heidelberg, Germany). Ultrapure water (18.2 MΩ cm) was obtained from a water purification system (Healforce, Shanghai, China).

2.2. Methods

2.2.1. Preparation of Solid lipid nanoparticles (SLN)

Solid lipid nanoparticles (SLN were produced by the hot ultra-sonication method as previously described (Magalhães et al., 2020). Briefly, a lipid phase comprising the solid lipid (Cetyl

palmitate) and the surfactant (Tween® 80) were melted at 70°C in a water bath (Variomag Electronicrührer, Labortechnik, Munich, Germany). A PBS solution heated at 70°C (4.4 mL), pH 8.2, was then poured into the lipid phase and the mixture was sonicated (VCX130, Sonics and Material Vibra-CellTM with a CV-18 probe; 115 Newtown CT, USA) at an amplitude frequency of 70% for 5 min. The formed nanoemulsion was then cooled at room temperature and stored at 4°C. To produce Mito-loaded SLN (SLN-Mito), Mito was dissolved in the PBS solution at the desired amount.

2.2.2. Experimental design

A 15-run, 3-level, 3-factor Box–Behnken design was employed to optimize the SLN nanoformulation, namely, to maximize the Entrapment Efficiency (EE%) and Loading Capacity (LC%) and minimize particle size (**Table 1**). The selected independent variables were the amount of Lipid (X_1), the amount of Surfactant (X_2), and the amount of Mito (X_3). For each independent variable, the low (-1), medium (0) and high (+1) levels were chosen according to preliminary SLN production studies (**Table 1**). The studied dependent variables were the size (Y_1), EE% (Y_2), and LC% (Y_3). The following equation gives the polynomial equation generated from the experimental design:

$$Y = b_0 + b_1X_1 + b_2X_2 + b_3X_3 + b_{12}X_1X_2 + b_{13}X_1X_3 + b_{23}X_2X_3 + b_{11}X_1^2 + b_{22}X_2^2 + b_{33}X_3^2$$

(**Equation 1**)

where Y is the dependent variable, b_0 is the intercept, X_1, X_2, X_3 are the coded levels of independent variables, and b_1 to b_{33} are the regression coefficients computed from the observed experimental values of Y. The terms X_1X_2 and X_i^2 (i = 1, 2 or 3) represent the interaction and quadratic terms, respectively. Data were statistically evaluated by analyzing the statistical significance of coefficients and multiple correlation coefficient (R^2) using ANOVA (*p* values < 0.05). The best-fitting experimental model was then selected. All the analyses were performed using the STATISTICA 10 software (Statsoft Power Solutions, Inc., Tulsa, OK, USA). After determining the optimum values for each independent variable, triplicates of the optimum nanoformulation were prepared and characterized and the observed values for each dependent variable were compared with the predicted values given by the Box-Behnken design.

2.2.3. Size, Nanoparticle concentration, Polydispersity Index, and Zeta Potential measurements

The size, polydispersity index (PDI), and zeta potential of the SLN were determined by dynamic light scattering (DLS) and electrophoretic light scattering (ELS) using a ZetaPALS analyzer (Brookhaven Instruments Corporation, Holtsville, NY, USA) operating at a scattering

angle of 90° at room temperature, with dust cut-off set to 30. SLN were diluted at a ratio of 1:300. For each sample, 6 runs of 10 cycles each were performed. All measurements were performed in triplicate. Detailed nanoparticle size distribution was also determined using nanoparticle tracking analysis (NTA, NanoSight NS300, Malvern Instruments, Worcestershire, UK) equipped with a 488 nm laser and a high sensitivity scientific CMOS camera. Samples were diluted at a ratio of 1:100,000, injected using a 1 mL sterile syringe in the viewing chamber and measured under constant flow (infusion rate of 50) at 24°C. Size measurements were obtained based on a 20s video captured with a camera level of 10 and a detection threshold of 5. For each sample, 5 size measurements were conducted. Data were analyzed using the NTA 3.4. software.

2.2.4. Entrapment Efficiency and Loading Capacity evaluation

EE% and LC% of the nanoformulations were measured using an indirect method of quantification. SLN were diluted (1:65), placed into centrifugal filter units (Amicon® Ultra Centrifugal Filters Ultracell-50 kDa, MERK Millipore, Ltd; Cork, Ireland) and centrifuged at 2851g (Allegra X-15R Centrifuge, Beckman Coulter, Fullerton, California) until the complete separation of the lipid and aqueous phase. The aqueous phase containing the non-entrapped Mito was recovered and the amount of Mito was quantified by UV-Vis spectrophotometry (Jasco V-660 Spectrophotometer, Software: Spectra Manager v.2, Jasco Corporation, USA) at 610 nm. A calibration curve was previously obtained using PBS pH 8.2 as a solvent.

EE% was determined by calculating the ratio between entrapped Mito (the difference between the total amount of Mito and the non-entrapped Mito) and the total amount of Mito as shown by the following equation:

$$\mathrm{EE\%} = \frac{\text{Total amount of Mito} - \text{Non entrapped Mito}}{\text{Total amount of Mito}} \times 100 \qquad \textbf{(Equation 2)}$$

LC% was obtained by calculating the ratio between the amount of entrapped Mito and the amount of lipid, surfactant, and entrapped Mito, as demonstrated by the following equation:

$$\mathrm{LC\%} = \frac{\mathrm{EE\%} \times \text{initial amount of Mito}}{\text{Amount of lipid} + \text{surfactant} + \mathrm{EE\%} \times \text{initial amount of Mito}} \qquad \textbf{(Equation 3)}$$

2.2.5. Transmission Electron Microscopy analysis

Morphology of the developed SLN was observed by Transmission Electron Microscopy (TEM). SLN were diluted 100 times in ultrapure water and placed over a cooper-mesh grid for 2 min. Negative staining was then performed using 0.75% (w/v) uranyl acetate for 30s. Samples were analyzed in TEM (TEM Jeol JEM-1400; JEOL Ltd., Tokyo, Japan) with an accelerating voltage of 80 kV.

2.2.6. Storage stability

The storage stability of the SLN was evaluated by performing periodic measurements of the size, PDI, zeta potential and EE% for 6 months. The stability study was conducted in triplicate for each formulation to achieve statistical significance.

2.2.7. *In vitro* release assay

The *in vitro* release of SLN-Mito was performed using a Slide-A-Lyzer dialysis device (Slide-A-Lyzer™ MINI Dialysis Device, MWCO 10kDa, Thermo Scientific™, MA, USA). The release profile was assessed in PBS at physiological pH (7.4) and in acetate buffer, pH 5.0, simulating the acidic endosomal compartment (Boedtkjer and Pedersen, 2020; Xu et al., 2019). SLN-Mito (0.5 mL) was added into the upper compartment of the dialysis device and 14 mL of the adequate buffer was added to the lower compartment. Devices were then placed in an incubator shaker (ES-60, Lan Technics, USA) at 100 RPM at 37°C for 24h. At regular intervals, aliquots of 1 mL were collected from the lower compartment and replaced with 1 mL of fresh buffer heated at 37°C. Mito content was then analyzed by UV-Vis spectrophotometry, as previously mentioned. Similarly, calibration curves were previously acquired in each buffer.

2.2.8. Hemolysis assay

Hemolysis assay was conducted using human blood collected from healthy donors in EDTA-coated tubes. Blood samples were obtained according to the principles of the declaration of Helsinki and were kindly donated by Serviço de Hematologia from Centro Hospitalar Universitário do Porto - Hospital de Santo António. Samples were centrifuged at 955g for 5 min at 4°C (Allegra X-15R Centrifuge, Beckman Coulter, Fullerton, California) to separate the red blood cells (RBCs) from the remaining blood components. RBCs were then washed 3 times with a 0.85% saline solution and diluted to a 4% (v/v) solution. Nanoformulations were diluted at the desired concentrations in saline solution. A solution of TX-100 (1% v/v) and saline solution were used as positive and negative controls, respectively. RBCs (100 µL) were then incubated with the samples (100 µL) in a 96-well plate at 37°C for 1h. After that, the supernatant was removed and the absorbance of hemoglobin was measured at 415 nm by UV-Vis spectroscopy using a plate reader (Biotek Instruments, Winooski, VT, USA). The percentage of hemolysis was calculated as follows:

$$Hemolysis\ \% = \frac{Abs\ (sample) - Abs\ (negative\ control)}{Abs\ (positive\ control) - Abs\ (negative\ control)} \times 100 \quad \textbf{(Equation 4)}$$

2.2.9. Cell viability: cytocompatibility and anti-cancer efficacy assessment in 2D *in vitro* cancer models

The effect of the nanoparticles on cell viability was evaluated using the resazurin assay as described previously (Lima-Sousa et al., 2020). The cytocompatibility of the unloaded nanoparticles was assessed both in normal cells (NHDF) and in the breast cancer cell line (MCF-7). The anti-cancer efficacy of SLN-Mito was evaluated in MCF-7 and AU-565 cells. Cells were seeded at a density of 1 x10^4 cells per well in 96-well plates and cultured in DMEM-F12 medium (MCF-7) or RPMI Medium 1640 (AU-565) supplemented with 10% (v/v) FBS and 1% (v/v) streptomycin/gentamycin in a humidified incubator (37°C, 5% CO_2) for 24h. Culture medium was then removed and replaced with different concentrations of each nanoformulation. After the incubation period (24 or 48h), the medium was removed and replaced by fresh culture medium containing 10% (v/v) of resazurin. After incubation for 4h in the dark (37°C, 5% CO_2), the fluorescence of resorufin (λ_{ex} = 560 nm; λ_{em} = 590 nm) was measured (Spectramax Gemini EM spectrofluorometer). Cells incubated with only culture medium were used as negative (K^-) control. The dose-response curves and the values of IC_{20}, IC_{50} and IC_{80} of SLN-Mito and free Mito were obtained using GraphPad Prism Software (v.6.0, GraphPad Software, CA, USA).

2.2.10. Penetration capacity evaluation in 3D *in vitro* breast cancer models

Heterotypic breast cancer spheroids were produced as previously described (Costa et al., 2018a; Mó et al., 2020). Briefly, agarose gel (2% w/v) was cast in a micro-mold (3D Petri Dish®, Microtissues Inc., Providence RI, USA) forming spherical micro well-containing structures. These structures were then placed in 12-well culture plates and sterilized by UV radiation for 3h. After that MCF-7 cells and NHDF, at a 1:1 cell ratio, were seeded at a density of 1 × 10^6 cells per agarose structure, forming 81 spheroids per structure. Spheroids were grown for 10 days in DMEM-F12 medium supplemented with 10% (v/v) FBS and 1% (v/v) streptomycin/gentamycin (37 °C, 5% CO_2), with medium replacement every 2 days. The penetration capacity of the nanoparticles in the heterotypic spheroids was evaluated according to previous studies (Costa et al., 2018b; Mó et al., 2020). Briefly, spheroids were incubated with free Mito and SLN-Mito at a concentration of 10 μM of Mito for 24h. After that, spheroids were fixed with paraformaldehyde 4% and visualized by Confocal Laser Scanning Microscopy (CSLM) using the fluorescence of Mito for imaging ($\lambda_{ex}/\lambda_{em}$ of 633/656-758 nm) in a Zeiss LSM 710 confocal microscope (Carl Zeiss SMT, Inc., Oberkochen, Germany). Z-stacks were collected with intervals of 30 μm and fluorescence intensity at different penetration depths was determined using ImageJ software.

2.2.11. Anti-cancer efficacy assessment in 3D *in vitro* breast cancer models

To assess the effect on spheroids' viability, different concentrations of SLN-Mito and free Mito diluted in culture medium were added followed by incubation for 48h. Heterotypic tumor spheroids were produced and maintained as detailed in section 2.2.10. The resazurin assay was then conducted, as described in **section 2.2.9**. Each condition was evaluated in a total of 30 spheroids. The therapeutic effect of the nanoparticles and free drug was also visualized using CLSM. With that purpose, spheroids were incubated with free Mito and SLN-Mito at a concentration of 21 μM of drug equivalents. After 24h, spheroids were stained with Calcein-AM and PI (according to the manufacturer's protocol) and visualized in CLSM (λ_{ex}/ λ_{em} of 488/493 –556 nm (Calcein-AM) and 561/566 –719 nm (PI)).

2.2.12. Statistical analysis

Statistical analysis was performed using Graphpad Prism6 Software (GraphPad Software Inc., San Diego, CA, USA). Unless stated otherwise, differences between control and treatment groups were assessed by one-way analysis of variance (ANOVA) using Dunnett's post-hoc test or two-way ANOVA using Tukey's test. A *p*-value lower than 0.05 was considered statistically significant. All data are expressed as mean ± SD.

3. Results and Discussion

3.1. Production optimization – experimental quality-by-design

Prior to the experimental design, initial studies were conducted to select the most suitable composition of Mito-loaded SLN. A lipid screening was performed by evaluating the solubility of mitoxantrone in different solid lipids at different ratios and solubility was visually estimated taking into account the presence of a clear blue solution and the lowest amount of drug crystals [3, 9] (**Table S1**). Pilot batches were then produced using the most promising solid lipids and after evaluating the physicochemical properties of the SLN (namely particle size, polydispersity and entrapment efficiency) (data not shown), cetyl palmitate was selected as the solid lipid for the nanoformulation. Additionally, the composition and pH of the aqueous phase was also selected. Other variables such as the speed and time of sonication were defined according to previous studies (Granja et al., 2017). Based on these preliminary studies, three factors (independent variables) were selected as the most relevant for the optimization of the nanoformulation: the amount of Lipid (X_1), the amount of Surfactant (X_2), and the amount of Mito (X_3).

A Box-Behnken design was then applied aiming to evaluate the effect of the selected factors on three different parameters (dependent variables), namely, size, EE%, and LC% and

ultimately determine the optimum production conditions according to the desired criteria. The implementation of this type of quality-by-design is a valuable tool in the development of drug delivery systems and in the pharmaceutical industry, enabling the optimization of different process parameters in a systematic, fast, and cost-effective way using a reduced number of experiments (Lawrence et al., 2014; Mishra et al., 2018).

Different combinations of the three factors were defined by the software, resulting in a total of 15 nanoformulations comprising 13 different nanoformulations and three replicates corresponding to the central point. The different combinations of factors and resulting parameters are summarized in **Table S2**.

The effects of each independent variable were analyzed via regression analysis. Based on the values of the correlation coefficient (R^2) between the experimental and the predicted values, the quadratic model was selected to proceed with the analysis (**Figure S1**). The significance of the model was statistically validated using ANOVA (**Table S3**, **S4,** and **S5**). The results of the regression analysis using the quadratic model for each response including the interaction coefficients of each independent variable and the corresponding *p-value* are summarized in **Table 1**.

Table 1. Regression analysis for the selected responses (size, EE% and LC%) using the quadratic model. Statistically significant values are represented in bold, *p*-value ≤ 0.05 with a 95% confidence interval.

	Size		EE%		LC%	
	Coeff.	*p-value*	Coeff.	*p-value*	Coeff.	*p-value*
Intercept	**224.250**	**0.000**	**86.665**	**0.000**	**1.496**	**0.000**
X_1	13.600	0.068	2.850	0.090	**-0.077**	**0.043**
X_1^2	3.462	0.315	0.230	0.754	0.012	0.405
X_2	**-19.283**	**0.036**	-3.669	0.057	**-0.161**	**0.010**
X_2^2	2.312	0.469	-1.301	0.179	-0.041	0.071
X_3	3.350	0.464	**-10.601**	**0.007**	**0.559**	**0.001**
X_3^2	1.312	0.665	0.576	0.464	**0.058**	**0.036**
X_1X_2	-2.900	0.621	1.4927	0.349	0.048	0.161
X_2X_3	-2.150	0.710	0.0004	0.100	-0.063	0.104
X_1X_3	-0.600	0.916	3.6642	0.097	0.050	0.149
R^2	0.962		0.989		0.999	

As shown in **Table 1** the values of the coefficients for each factor are either negative or positive, which indicates an antagonist or synergistic effect on the response, respectively. Interaction terms are represented by two factors and quadratic relationships are represented by higher order terms. A visual representation of the statistically significant effects of the factors on each response is depicted in the response contour plots in **Figure S2**.

The regression analysis demonstrated that the particle size was significantly affected by the amount of surfactant (X_2). The negative sign of the coefficient indicates an inverse relationship, meaning that increasing the amount of surfactant results in a decrease in particle size. This

effect may be attributed to a reduction in the interfacial tension between the lipid and the external phase induced by the surfactant, leading to the stabilization and formation of smaller particles, which is in agreement with previous studies (Ferreira et al., 2015; Magalhães et al., 2020).

The amount of drug also had a significant negative effect on EE%. This may occur due to a limited capacity of the lipid matrix to accommodate the drug. This suggests that adding increasing amounts of drug above this capacity increases the amount of non-entrapped drug which reduces the EE% (Gidwani and Vyas, 2016; Joseph et al., 2017).

LC% was significantly affected by the amount of lipid, surfactant, Mito, and the quadratic term of the amount of Mito. Both lipid and surfactant have a significant negative effect on LC%, which is expected as there is an inversely proportional relationship between them, as depicted in **Equation 3**. The amount of Mito and the quadratic term of this factor, as expected, had a positive effect on LC%.

As shown in **Table 1** and **Figure S1**, a good correlation (R^2) was obtained for all the regression equations for each response, indicating a good fitting of the quadratic model. The optimum nanoformulation composition was then assessed using the prediction and profiling function on the STATISTICA 10 software. The criteria established for the optimum nanoformulation consisted of maximum EE% and LC% and minimum particle size. To validate the optimization procedure and the prediction ability of the model, the nanoformulation with the optimum composition (210 mg of Solid lipid, 70 mg of surfactant, and 4.5 mg of Mito) was produced in triplicate and characterized. As shown in **Table 2** a good agreement between the predicted and observed values was obtained for all the responses, which validates the experimental design and the robustness of the model for the optimization of the nanoformulation.

Table 2. Predicted versus experimental values obtained for each response (size, EE%, and LC%) of the optimum nanoformulation

	Predicted	Experimental
Size (nm)	219	230 ± 17
EE%	99	93 ± 6
LC%	1.6	1.5 ± 0.1

3.2. Nanoparticle physicochemical characterization

After validation of the experimental design, three replicates of the optimal (SLN-Mito) and corresponding unloaded nanoformulations (SLN) were produced and characterized in terms of size, PDI, Zeta potential, EE% and LC% (**Table 3**). The results of particle size performed using DLS suggest that the entrapment of Mito did not significantly affect the hydrodynamic diameter of the nanoparticles, which remained around 230 nm. A more detailed size

distribution analysis was performed using NTA (**Figure S3)**, which is a relatively recent technique that can complement the results obtained by DLS (Filipe et al., 2010). A mean particle size of 155 ± 2 and 153 ± 3 nm, for SLN and SLN-Mito, respectively, were obtained by NTA, which are lower than the values obtained using DLS. This difference can be explained by the fact that DLS measurements are frequently biased towards the presence of larger nanoparticles, even at a very small number, as the light scattering intensity is more affected by the size than by the number of nanoparticles (Amaro-Gahete et al., 2019). NTA, in contrast, measures the hydrodynamic diameter by tracking each nanoparticle individually through image analysis, providing a more detailed characterization of size distribution (Amaro-Gahete et al., 2019; Fan et al., 2015). DLS, on the other hand, is a less time-consuming and non-destructive technique (Amaro-Gahete et al., 2019).

Overall, these results suggest that the nanoparticles have a suitable size for intravenous administration and tumor passive accumulation through the enhanced permeability and retention (EPR) effect (Attia et al., 2019; Huang et al., 2021; Singh and Lillard Jr, 2009). The values of PDI were below 0.2, which indicates the presence of an homogeneous population for lipid-based nanocarriers (Danaei et al., 2018). Zeta potential for both SLN and SLN-Mito were close to neutral (-3 ± 1 mV), which is expected due to the use of a dispersion media of physiologic ionic strength (PBS), which is higher than double deionized water (Brown et al., 2016). Similar results have been reported elsewhere (Goutayer et al., 2010; Rajapaksa et al., 2010). This can be an advantage in cancer therapy applications since neutral or slightly negative surface charges are associated with a limited uptake by the reticuloendothelial system, longer circulation half-lives, and higher tumor accumulation following intravenous administration (Blanco et al., 2015; Ernsting et al., 2013). Finally, a high value of EE% (93%) was obtained, corroborating the predicted results from the Box-Behnken design.

Table 3. Physicochemical characterization of the optimized SLN (SLN-Mito) and corresponding unloaded SLN (SLN): size (determined by DLS), PDI, Zeta potential, EE% and LC%. Data are expressed as mean ± SD (n = 3).

	Size (nm)	PDI	Zeta potential (mV)	EE%	LC%
SLN	226 ± 17	0.14 ± 0.02	-4 ± 1	-	-
SLN-Mito	230 ± 17	0.16 ± 0.01	-3 ± 1	93 ± 6	1.5 ± 0.1

Nanoparticle morphology and size distribution were also evaluated using TEM (**Figure 1)**. Both nanoformulations present spherical morphology, absence of particle aggregation, and particle size in agreement with the DLS and NTA measurements.

3.3. Storage stability

Storage stability was evaluated over a period of 24 weeks (6 months). Nanoformulations were kept at 4°C, and periodic assessments of their physiochemical properties were performed. As shown in **Figure 2A**, particle size remained stable during the 6 months of the study, which suggests the absence of aggregate formation during storage. **Figure 2B** shows the variation of PDI and corroborates these results, showing that, although a slight increase can be observed, the values of this parameter remained below 0.2 after 6 months of storage, which is an indicator of a homogeneous population for lipid-based nanocarriers (Danaei et al., 2018). An increase in the zeta potential absolute values occurred in the last two time-points of the study. Nevertheless, all the values remained slightly negative, below -10 mV (**Figure 2C**). Encapsulation efficiency remained above 90% for at least 6 months, demonstrating the absence of drug leaking during storage (**Figure 2D**). These results support that the developed nanoformulations are stable in suspension for at least 6 months.

3.4. *In vitro* release study

The release of Mito from the SLN was assessed using the dialysis method at pH 7.4 and 5.0 to simulate the physiological environment and the endosomal compartment, respectively (Kim et al., 2014). The cumulative percentages of Mito release are presented in **Figure 3** where a pH-dependency can be observed. At pH 7.4, SLN releases Mito in a controlled manner, with more than 60% of drug remaining encapsulated after 24h, suggesting that only a limited amount of drug will be released in physiological environment such as the bloodstream and other normal tissues. A much faster release is observed at pH 5.0, characteristic of the acidic endosomal compartment. To evaluate the mechanism of drug release from the SLN at the two pH, data were fitted to different drug release models including zero order, first order, Higuchi, Hixson-Crowell and Korsmeyer-Peppas. The correlation coefficients (R^2) and the release rate constants (k) obtained for each model is presented in **Table S6**. Based on these values, the Higuchi model was found to be the model that best described the release kinetics of the drug at both pH conditions. This suggests that the release of Mito occurs mainly by a diffusion-controlled process [1]. The release rate constant (k_H) obtained for the two studied pH also clearly demonstrates a higher drug release rate at pH 5.0 than at pH 7.4.

Overall, these data show that SLN can release Mito at a much faster rate at acidic than at physiological pH. This suggests that once in the human body, SLN will presumably have a controlled drug release in the bloodstream and normal healthy tissues, which can reduce the systemic toxic effects of the free drug. Additionally, a much faster release will occur in acidic environments such as the tumor tissue and endosomal compartment, where the free drug can exert its effect. These findings support that the developed nanoformulations are suitable carriers for the delivery of Mito to tumor tissues.

3.5. Hemolysis assay

The hemocompatibility of the SLN was assessed through a hemolysis assay using human RBCs collected from 3 healthy donors. Hemolysis was assessed in a concentration range from 1 to 24 mg/mL of lipid after incubation for 1h. As shown in **Figure 4**, all values of hemolysis were lower than 5% even at very high concentrations of lipid, with the maximum of hemolysis reaching only 3%. These findings support that the developed SLN are non-toxic according to ISO 10993-4 (Standard, 2017) and, therefore, safe for intravenous administration.

3.6. Cytocompatibility assessment

The safety of the SLN was further evaluated through the assessment of their cytocompatibility for both normal and cancer cells. As depicted in **Figure 5A**, unloaded SLN did not induce any reduction in cell viability up to 900 µg/mL of lipid after incubation for 24 and 48h in human fibroblasts. These results are in agreement with previous studies where concentrations up to 1000 µg/mL of similar types of nanoparticles were found to be cytocompatible for NHDF cells after 24h and 48h incubation (Doktorovova et al., 2014; Ruktanonchai et al., 2009). In the MCF-7 breast cancer cell line (**Figure 5B**), SLN were found to be cytocompatible for 24h at the highest concentration tested. After 48h of incubation, however, SLN were cytocompatible up to a concentration of 500 µg/mL of lipid. An IC_{50} of 605 µg/mL of lipid was determined for this incubation period (**Figure S6**). This value is comparable or higher than others reported in the literature for similar types of nanoparticles in MCF-7 cells following 48h incubation, demonstrating the high cytocompatibility of the produced SLN (Abbasalipourkabir et al., 2011; Miao et al., 2013; Ying et al., 2011).

3.7. Anti-cancer efficacy on 2D *in vitro* breast cancer models

The anti-cancer efficacy was evaluated in MCF-7 cell lines for 24 and 48h (Figure **6A** and **6B**). As expected, a decrease in breast cancer cell viability is observed with increasing Mito concentrations. It is noteworthy that SLN-Mito have a significantly higher anti-tumoral effect comparing to the free drug. After 24h of incubation, SLN-Mito elicit a significantly higher cancer cell death when compared with free Mito at concentrations of 21 µM (corresponding to 500 µg/mL of lipid) or higher, with only 14% of cell viability at a concentration of 29 µM and almost full eradication at the highest concentrations tested. This effect cannot be attributed to any intrinsic toxicity of the lipid matrix, as in this range of concentrations, all the corresponding unloaded SLN were found to be cytocompatible, as highlighted in **Figure 5**. After 48h of incubation, a similar trend was observed with SLN-Mito significantly improving MCF-7 cells' death at concentrations of 10 µM or higher, achieving almost full eradication at a concentration of 21 µM, corresponding to a lipid concentration of 500 µg/mL, which was found to be cytocompatible (**Figure 6B**). To further demonstrate the anti-cancer efficacy of the

nanosystem, the effects of the nanoformulation on cell viability were also evaluated in the HER-2-positive breast cancer cell line Au-565 (**Figures S4** and **S5).** A similar trend can be observed, with comparable or higher anti-cancer activity induced by SLN-Mito comparing to the free drug.

Based on the results obtained in MCF-7 cells, dose-response curves were plotted (**Figure S7**) and values of IC_{50}, IC_{20}, and IC_{80} were calculated (**Table S7).** IC_{50} values for free Mito and SLN-Mito were found to be 25 and 21 μM after 24h incubation and 13 μM and 10 μM after 48h incubation, which further supports the higher anti-cancer activity of SLN-Mito comparing to the free drug.

Comparing to other mitoxantrone nanodelivery vehicles reported in the literature, the SLN developed in this study demonstrated a higher capacity to improve the anti-cancer efficacy of Mito(Ma et al., 2011; Sargazi et al., 2018). For instance, Sargazi *et al.* developed hyaluronan PEGylated magnetic nanoparticles conjugated with Mito and showed that after 48h and 72h the nanosystem could not inhibit MCF-7 cell viability, in contrast to what occurred with the free drug at a concentration range of 25-400 μM (Sargazi et al., 2018). Ma *et al.* showed a similar or lower anti-tumor efficacy of Mito-loaded mesoporous silica nanoparticles comparing to free Mito up to 10 μg/mL (22 μM) after 24h incubation (Ma et al., 2011). Other works have developed Mito nanodelivery systems reporting values of IC_{50} relatively lower than the ones described in our study (Pedrosa et al., 2015; Wang et al., 2018). Nevertheless, in one of these studies the nanosystem comprising nanoliposomes could not improve the efficacy of the free drug (Pedrosa et al., 2015), while in another work, chitosan/hyaluronate polyelectrolyte nanoparticles did not induce full eradication of MCF-7 cells even after treatment with high concentrations of Mito (45 μM) (Wang et al., 2018).

Overall, our results clearly demonstrate the capacity of the developed SLN to improve the anti-tumoral activity of Mito in 2D *in vitro* breast cancer models.

3.8. Penetration and therapeutic efficacy on 3D *in vitro* breast cancer models

Although 2D cell monolayers offer a quick and relatively easy way to assess the toxicity and anti-cancer efficacy of nanomedicines, the complexity of the solid tumor microenvironment cannot be replicated using these models (Costa et al., 2016; Lu and Stenzel, 2018; Nath and Devi, 2016). In contrast, 3D *in vitro* cancer models, such as spheroids, can replicate several features of the *in vivo* solid tumors in terms of heterogeneity, cell and extracellular matrix interactions, pH, nutrient access, and drug permeability. For these reasons, spheroids are considered valuable tools for drug and nanomedicine screening and prediction of their outcomes *in vivo* (Costa et al., 2016; Lu and Stenzel, 2018; Nath and Devi, 2016).

First, the penetration of the nanoparticles was evaluated through CLSM using the fluorescence of Mito for visualization. As shown in **Figure 7,** fluorescence signals were found at different penetration depths, demonstrating that the nanoparticles are able to cross the physical barrier created by the spheroid. The plots of fluorescence intensity showed that the vast majority of the SLN could effectively penetrate at the outer layers of the spheroid, with some of them being able to reach the core, as shown by the weak fluorescence signal obtained from the inner sections. These results are in agreement with other works where it was demonstrated that the inner layer of the spheroid is less affected by the effect of nanomedicines (Lee et al., 2009). Such is a consequence of the higher resistance of spheroids to nanomedicines' penetration (*e.g.* due to increased cell-cell interactions) (Lee et al., 2009). Overall, SLN-Mito showed a similar capacity to the free drug to penetrate the spheroid.

To evaluate the anti-cancer efficacy, different concentrations of SLN-Mito and corresponding free drug were tested in the heterotypic breast cancer spheroids (**Figure 8**). A dose-dependent response was obtained with similar effects induced by the free drug and SLN-Mito (approximately 66% of viability) at the lowest concentration tested (10 μM). At a concentration of 21 μM, SLN-Mito elicited a significantly higher cell death with only 27% viable cells remaining compared to 41% induced by the free drug. For the highest concentrations tested, anti-cancer effects were similar for both treatments with approximately 9% of cell viability obtained at the highest concentration tested. These results contrast to what occurred in the 2D cultures (**Figure 6B**), where SLN-Mito reduced cell viability to 44% compared to 65% of the free drug at a concentration of 10 μM, and at 21 μM or higher concentrations almost full eradication (4% cell viability) was achieved after treatment with SLN-Mito. This can be attributed to the high complexity of the 3D model, which makes it less susceptible to anti-cancer therapeutics when compared to cells cultured in monolayer. For instance, the limited amount of oxygen and nutrients in the tumor spheroid may lead to an enhanced number of quiescent cells, which have a higher therapeutic resistance. Moreover, heterotypic spheroids were used in this study to better mimic the heterogeneity of the tumor tissue. This may further increase the therapeutic resistance of the spheroid due to increased secretion of cytokines and proliferation factors resultant from the interaction between fibroblasts and MCF-7 cells (Nunes et al., 2019).

The effect of 21 μM of both free Mito and SLN-Mito (of Mito equivalents) was further evaluated by staining with Calcein-AM/PI and visualization using CLSM. As shown in **Figure 9**, in the negative control spheroids present a regular spherical morphology and are composed by an outer layer with living proliferating cells (stained with Calcein-AM) and a necrotic core, as predicted for these types of spheroids (Wallace and Guo, 2013). A much higher amount of PI-stained cells is visible following both treatments when compared to the control. When comparing the two treatments it is possible to observe that SLN-Mito induced a higher amount

of PI-stained cells than the free drug, which is in agreement with the anti-cancer activity results shown in **Figure 8**.

Overall, these results highlight the efficacy of the developed nanosystem for the management of breast cancer demonstrating its capacity to penetrate the breast cancer tumor spheroid and to induce a high anti-tumoral effect, comparable to the free drug.

4. Conclusion

In the present work, SLN were produced for the entrapment of the chemotherapeutic drug Mito, using an organic-solvent free and low-cost production method. Particle size, EE%, and LC% were then optimized in a cost-effective way through the application of a Box-Behnken quality-by-design. Overall, SLN presented an adequate size for intravenous administration and tumor passive targeting and an EE% higher than 90% and remained stable for at least 6 months. The *in vitro* release studies suggest that following 24h after intravenous administration, a controlled release of Mito will occur at physiological pH such as the bloodstream and normal tissues, which may limit the drugs' systemic toxicity. On the other hand, a much faster release occurs at acidic pH, such as the tumor environment and the cell endosomal compartment, where the free drug can exert its effects. Hemolysis assay conducted using human RBCs revealed that the nanoformulation in non-hemolytic even at high concentrations, further supporting its suitability for intravenous administration. Additionally, the biocompatibility of the lipid vehicle was assessed in both normal (NHDF) and cancer cells (MCF-7) showing very high tolerability even after treatment with high concentrations of lipid. The therapeutic efficacy of the nanoformulation was then evaluated in MCF-7 cells, where it was found that SLN could effectively increase the therapeutic efficacy of Mito, as shown by the values of IC_{50} of the free drug versus SLN-Mito following 24h and 48h incubation. Finally, to better mimic the complexity of the tumor microenvironment, heterotypic spheroids were developed and the anti-tumoral effect of the nanoformulation was assessed. The results demonstrated that the nanoformulation was able to elicit a high anti-tumoral effect and effectively cross the physical barrier created by the tumor spheroid.

Overall, the results presented in this work highlight that the developed SLN are promising Mito nanocarriers for the treatment of breast cancer. Their simple and low-cost production methods and their higher stability in comparison to other clinical available nanocarriers, such as liposomes, may benefit their clinical translation in the near future.

Acknowledgments

This work received financial support from PT national funds (FCT/MCTES, Fundação para a Ciência e Tecnologia and Ministério da Ciência, Tecnologia e Ensino Superior) through the project UIDB/50006/2020 (LAQV-REQUIMTE). This work was also financed by CENTRO-01-

0145-FEDER-028989 and POCI-01-0145-FEDER-031462. Andreia Granja acknowledges FCT (Fundação para a Ciência e Tecnologia) and ESF (European Social Fund) for her PhD grant SFRH/BD/130147/2017. Rita Lima-Sousa and Cátia G. Alves acknowledge funding from individual PhD fellowships from FCT (SFRH/BD/144922/2019 and SFRH/BD/145386/2019). Duarte de Melo-Diogo acknowledges CENTRO-01-0145-FEDER-028989 for the funding given in the form of a research contract. Marina Pinheiro thanks FCT for financial support through program DL 57/2016—Norma transitória (SFRH/BPD/99124/2013). Célia T. Sousa thanks FCT for financial support through the Investigador FCT program (contract no. IF/01159/2015) and the UE's Horizon 2020 research and innovation program under the Marie Sklodowska-Curie grant no. 734801. The authors are also grateful to Dr. Rui Fernandes (Histology and Electron Microscopy Service – Instituto de Investigação e Inovação em Saúde, Universidade do Porto) for expertise and technical assistance with transmission electron microscopy.

References

Abbasalipourkabir, R., Salehzadeh, A., Abdullah, R., 2011. Cytotoxicity effect of solid lipid nanoparticles on human breast cancer cell lines. Biotechnology 10, 528-533.

Amaro-Gahete, J., Benítez, A., Otero, R., Esquivel, D., Jiménez-Sanchidrián, C., Morales, J., Caballero, Á., Romero-Salguero, F.J., 2019. A comparative study of particle size distribution of graphene nanosheets synthesized by an ultrasound-assisted method. Nanomaterials 9, 152.

Attia, M.F., Anton, N., Wallyn, J., Omran, Z., Vandamme, T.F., 2019. An overview of active and passive targeting strategies to improve the nanocarriers efficiency to tumour sites. Journal of Pharmacy and Pharmacology 71, 1185-1198.

Bai, X., Ni, J., Beretov, J., Graham, P., Li, Y., 2018. Cancer stem cell in breast cancer therapeutic resistance. Cancer Treatment Reviews 69, 152-163.

Blanco, E., Ferrari, M., 2014. Emerging nanotherapeutic strategies in breast cancer. The Breast 23, 10-18.

Blanco, E., Shen, H., Ferrari, M., 2015. Principles of nanoparticle design for overcoming biological barriers to drug delivery. Nature biotechnology 33, 941-951.

Boedtkjer, E., Pedersen, S.F., 2020. The acidic tumor microenvironment as a driver of cancer. Annual review of physiology 82, 103-126.

Brown, M.A., Goel, A., Abbas, Z., 2016. Effect of electrolyte concentration on the stern layer thickness at a charged interface. Angewandte Chemie 128, 3854-3858.

Costa, E.C., Moreira, A.F., de Melo-Diogo, D., Correia, I.J., 2018a. ClearT immersion optical clearing method for intact 3D spheroids imaging through confocal laser scanning microscopy. Optics & Laser Technology 106, 94-99.

Costa, E.C., Moreira, A.F., de Melo-Diogo, D., Correia, I.J., 2018b. Polyethylene glycol molecular weight influences the Clear T2 optical clearing method for spheroids imaging by confocal laser scanning microscopy. Journal of biomedical optics 23, 055003.

Costa, E.C., Moreira, A.F., de Melo-Diogo, D., Gaspar, V.M., Carvalho, M.P., Correia, I.J., 2016. 3D tumor spheroids: an overview on the tools and techniques used for their analysis. Biotechnology advances 34, 1427-1441.

Danaei, M., Dehghankhold, M., Ataei, S., Hasanzadeh Davarani, F., Javanmard, R., Dokhani, A., Khorasani, S., Mozafari, M., 2018. Impact of particle size and polydispersity index on the clinical applications of lipidic nanocarrier systems. Pharmaceutics 10, 57.

Doktorovova, S., Souto, E.B., Silva, A.M., 2014. Nanotoxicology applied to solid lipid nanoparticles and nanostructured lipid carriers–a systematic review of in vitro data. European Journal of Pharmaceutics and Biopharmaceutics 87, 1-18.

Ernsting, M.J., Murakami, M., Roy, A., Li, S.-D., 2013. Factors controlling the pharmacokinetics, biodistribution and intratumoral penetration of nanoparticles. Journal of controlled release : official journal of the Controlled Release Society 172, 782-794.

Fan, Y., Sahdev, P., Ochyl, L.J., Akerberg, J.J., Moon, J.J., 2015. Cationic liposome–hyaluronic acid hybrid nanoparticles for intranasal vaccination with subunit antigens. Journal of controlled release 208, 121-129.

Feng, L., Mumper, R.J., 2013. A critical review of lipid-based nanoparticles for taxane delivery. Cancer letters 334, 157-175.

Ferreira, M., Chaves, L.L., Lima, S.A.C., Reis, S., 2015. Optimization of nanostructured lipid carriers loaded with methotrexate: a tool for inflammatory and cancer therapy. International journal of pharmaceutics 492, 65-72.

Filipe, V., Hawe, A., Jiskoot, W., 2010. Critical evaluation of Nanoparticle Tracking Analysis (NTA) by NanoSight for the measurement of nanoparticles and protein aggregates. Pharmaceutical research 27, 796-810.

Gidwani, B., Vyas, A., 2016. Preparation, characterization, and optimization of altretamine-loaded solid lipid nanoparticles using Box-Behnken design and response surface methodology. Artificial cells, nanomedicine, and biotechnology 44, 571-580.

Goutayer, M., Dufort, S., Josserand, V., Royère, A., Heinrich, E., Vinet, F., Bibette, J., Coll, J.-L., Texier, I., 2010. Tumor targeting of functionalized lipid nanoparticles: assessment by in vivo fluorescence imaging. European Journal of Pharmaceutics and Biopharmaceutics 75, 137-147.

Granja, A., Vieira, A.C., Chaves, L.L., Nunes, C., Neves, A.R., Pinheiro, M., Reis, S., 2017. Folate-targeted nanostructured lipid carriers for enhanced oral delivery of epigallocatechin-3-gallate. Food Chemistry 237, 803-810.

Huang, D., Sun, L., Huang, L., Chen, Y., 2021. Nanodrug Delivery Systems Modulate Tumor Vessels to Increase the Enhanced Permeability and Retention Effect. Journal of Personalized Medicine 11, 124.

Imanparast, A., Bakhshizadeh, M., Salek, R., Sazgarnia, A., 2018. Pegylated hollow gold-mitoxantrone nanoparticles combining photodynamic therapy and chemotherapy of cancer cells. Photodiagnosis and photodynamic therapy 23, 295-305.

Joseph, E., Reddi, S., Rinwa, V., Balwani, G., Saha, R., 2017. Design and in vivo evaluation of solid lipid nanoparticulate systems of Olanzapine for acute phase schizophrenia treatment: Investigations on antipsychotic potential and adverse effects. European Journal of Pharmaceutical Sciences 104, 315-325.

Kim, S.W., Oh, K.T., Youn, Y.S., Lee, E.S., 2014. Hyaluronated nanoparticles with pH-and enzyme-responsive drug release properties. Colloids and Surfaces B: Biointerfaces 116, 359-364.

Lasa-Saracibar, B., Estella-Hermoso de Mendoza, A., Guada, M., Dios-Vieitez, C., Blanco-Prieto, M.J., 2012. Lipid nanoparticles for cancer therapy: state of the art and future prospects. Expert opinion on drug delivery 9, 1245-1261.

Lawrence, X.Y., Amidon, G., Khan, M.A., Hoag, S.W., Polli, J., Raju, G., Woodcock, J., 2014. Understanding pharmaceutical quality by design. The AAPS journal 16, 771-783.

Lee, J., Lilly, G.D., Doty, R.C., Podsiadlo, P., Kotov, N.A., 2009. In vitro toxicity testing of nanoparticles in 3D cell culture. Small 5, 1213-1221.

Lima-Sousa, R., de Melo-Diogo, D., Alves, C.G., Cabral, C.S., Miguel, S.P., Mendonça, A.G., Correia, I.J., 2020. Injectable in situ forming thermo-responsive graphene based hydrogels for cancer chemo-photothermal therapy and NIR light-enhanced antibacterial applications. Materials Science and Engineering: C 117, 111294.

Lu, B., Xiong, S.-B., Yang, H., Yin, X.-D., Chao, R.-B., 2006. Solid lipid nanoparticles of mitoxantrone for local injection against breast cancer and its lymph node metastases. European journal of pharmaceutical sciences 28, 86-95.

Lu, H., Stenzel, M.H., 2018. Multicellular tumor spheroids (MCTS) as a 3D in vitro evaluation tool of nanoparticles. Small 14, 1702858.

Luengo-Fernandez, R., Leal, J., Gray, A., Sullivan, R., 2013. Economic burden of cancer across the European Union: a population-based cost analysis. The lancet oncology 14, 1165-1174.

Ma, Y., Zhou, L., Zheng, H., Xing, L., Li, C., Cui, J., Che, S., 2011. pH-responsive mitoxantrone (MX) delivery using mesoporous silica nanoparticles (MSN). Journal of Materials Chemistry 21, 9483-9486.

Magalhães, J., L Chaves, L., C Vieira, A., G Santos, S., Pinheiro, M., Reis, S., 2020. Optimization of Rifapentine-Loaded Lipid Nanoparticles Using a Quality-by-Design Strategy. Pharmaceutics 12, 75.

Mei, K.-C., Liao, Y.-P., Jiang, J., Chiang, M., Khazaieli, M., Liu, X., Wang, X., Liu, Q., Chang, C.H., Zhang, X., 2020. Liposomal delivery of mitoxantrone and a cholesteryl indoximod prodrug provides effective chemo-immunotherapy in multiple solid tumors. ACS nano 14, 13343-13366.

Mei, L., Zhang, Z., Zhao, L., Huang, L., Yang, X.-L., Tang, J., Feng, S.-S., 2013. Pharmaceutical nanotechnology for oral delivery of anticancer drugs. Advanced drug delivery reviews 65, 880-890.

Miao, J., Du, Y.-Z., Yuan, H., Zhang, X.-g., Hu, F.-Q., 2013. Drug resistance reversal activity of anticancer drug loaded solid lipid nanoparticles in multi-drug resistant cancer cells. Colloids and Surfaces B: Biointerfaces 110, 74-80.

Minchinton, A.I., Tannock, I.F., 2006. Drug penetration in solid tumours. Nature Reviews Cancer 6, 583-592.

Mishra, V., Thakur, S., Patil, A., Shukla, A., 2018. Quality by design (QbD) approaches in current pharmaceutical set-up. Expert opinion on drug delivery 15, 737-758.

Mó, I., Alves, C.G., de Melo-Diogo, D., Lima-Sousa, R., Correia, I.J., 2020. Assessing the Combinatorial Chemo-Photothermal Therapy Mediated by Sulfobetaine Methacrylate-Functionalized Nanoparticles in 2D and 3D In Vitro Cancer Models. Biotechnology Journal 15, 2000219.

Nath, S., Devi, G.R., 2016. Three-dimensional culture systems in cancer research: Focus on tumor spheroid model. Pharmacology & therapeutics 163, 94-108.

Nunes, A.S., Barros, A.S., Costa, E.C., Moreira, A.F., Correia, I.J., 2019. 3D tumor spheroids as in vitro models to mimic in vivo human solid tumors resistance to therapeutic drugs. Biotechnology and bioengineering 116, 206-226.

Pedrosa, L.R.C., Ten Hagen, T.L., Süss, R., van Hell, A., Eggermont, A.M., Verheij, M., Koning, G.A., 2015. Short-chain glycoceramides promote intracellular mitoxantrone delivery from novel nanoliposomes into breast cancer cells. Pharmaceutical research 32, 1354-1367.

Posner, L.E., Dukart, G., Goldberg, J., Bernstein, T., Cartwright, K., 1985. Mitoxantrone: an overview of safety and toxicity. Investigational new drugs 3, 123-132.

Rajapaksa, T.E., Bennett, K.M., Hamer, M., Lytle, C., Rodgers, V.G., Lo, D.D., 2010. Intranasal M cell uptake of nanoparticles is independently influenced by targeting ligands and buffer ionic strength. Journal of Biological Chemistry 285, 23739-23746.

Rossato, L.G., Costa, V.M., de Pinho, P.G., Arbo, M.D., de Freitas, V., Vilain, L., de Lourdes Bastos, M., Palmeira, C., Remiao, F., 2013. The metabolic profile of mitoxantrone and its relation with mitoxantrone-induced cardiotoxicity. Archives of toxicology 87, 1809-1820.

Ruktanonchai, U., Sakulkhu, U., Bejrapha, P., Opanasopit, P., Bunyapraphatsara, N., Junyaprasert, V., Puttipipatkhachorn, S., 2009. Effect of lipid types on physicochemical characteristics, stability and antioxidant activity of gamma-oryzanol-loaded lipid nanoparticles. Journal of microencapsulation 26, 614-626.

Sargazi, A., Shiri, F., Keikha, S., Majd, M.H., 2018. Hyaluronan magnetic nanoparticle for mitoxantrone delivery toward CD44-positive cancer cells. Colloids and Surfaces B: Biointerfaces 171, 150-158.

Singh, R., Lillard Jr, J.W., 2009. Nanoparticle-based targeted drug delivery. Experimental and molecular pathology 86, 215-223.

Standard, I., 2017. ISO 10993-4: Biological Evaluation of Medical Devices Part 4—Selection of Tests for Interactions with Blood. International Organization for Standardization: Geneva, Switzerland.

Sun, L., Legood, R., dos-Santos-Silva, I., Gaiha, S.M., Sadique, Z., 2018. Global treatment costs of breast cancer by stage: a systematic review. PloS one 13, e0207993.

Sung, H., Ferlay, J., Siegel, R.L., Laversanne, M., Soerjomataram, I., Jemal, A., Bray, F., 2021. Global cancer statistics 2020: GLOBOCAN estimates of incidence and mortality worldwide for 36 cancers in 185 countries. CA: a cancer journal for clinicians 71, 209-249.

Varadwaj, P., Misra, K., Sharma, A., Kumar, R., 2010. Mitoxantrone: an agent with promises for anticancer therapies. Electronic Journal of Biology 6, 36-42.

Wallace, D.I., Guo, X., 2013. Properties of tumor spheroid growth exhibited by simple mathematical models. Frontiers in oncology 3, 51-51.

Wang, J., Asghar, S., Jin, X., Chen, Z., Huang, L., Ping, Q., Zong, L., Xiao, Y., 2018. Mitoxantrone-loaded chitosan/hyaluronate polyelectrolyte nanoparticles decorated with amphiphilic PEG derivates for long-circulating effect. Colloids and Surfaces B: Biointerfaces 171, 468-477.

Wang, L., Zhao, Y., Li, T., Cao, J., Du, Y., Tao, Z., Peng, W., Wang, B., Zhang, J., Wang, Z., 2020. Efficacy and safety of liposomal mitoxantrone (Lipo-MIT) in advanced breast cancer (ABC): A randomized, open label, active-controlled, single-center, phase II clinical trial. American Society of Clinical Oncology.

Wicki, A., Witzigmann, D., Balasubramanian, V., Huwyler, J., 2015. Nanomedicine in cancer therapy: challenges, opportunities, and clinical applications. Journal of controlled release : official journal of the Controlled Release Society 200, 138-157.

Xu, Y., Shan, Y., Zhang, Y., Yu, B., Shen, Y., Cong, H., 2019. Multifunctional Fe3O4@ C-based nanoparticles coupling optical/MRI imaging and pH/photothermal controllable drug release as efficient anti-cancer drug delivery platforms. Nanotechnology 30, 425102.

Ying, X.-Y., Cui, D., Yu, L., Du, Y.-Z., 2011. Solid lipid nanoparticles modified with chitosan oligosaccharides for the controlled release of doxorubicin. Carbohydrate polymers 84, 1357-1364.

Zhuang, Y.-g., Xu, B., Huang, F., Wu, J.-j., Chen, S., 2012. Solid lipid nanoparticles of anticancer drugs against MCF-7 cell line and a murine breast cancer model. Die Pharmazie-An International Journal of Pharmaceutical Sciences 67, 925-929.

Figure captions

Figure 1. TEM photographs of SLN (**A**) and SLN-Mito (**B**), Magnification 50000X.

Figure 2. Storage stability of (**A**) particle size, (**B**) PDI, (**C**) zeta potential and (**D**) EE% over 24 weeks at 4°C. Data are expressed as mean ± SD (n = 3). Differences between control (time point 0) and other time points were performed using One-way ANOVA followed by Dunnett's test (*) denotes statistically significant differences relative to the correspondent week 0. *p<0.05, **p<0.01.

Figure 3. Cumulative release of Mito at physiological (7.4) and acidic (5.0) pH. Data are expressed as mean ± SD (n = 3).

Figure 4. *In vitro* hemolysis assay of SLN and SLN-Mito. (**A**) Image of the samples treated with the highest concentration (24 mg/mL) tested of SLN and SLN-Mito and controls - negative (saline solution) and positive (TX-100 - 1% v/v) following 1h incubation. (**B**) Graphic representation of the concentration-dependent hemolysis induced by SLN and SLN-Mito. Data are expressed as mean ± SD (n = 3).

Figure 5. Effect of unloaded SLN on the viability of NHDF (**A**) and breast cancer cell line MCF-7 (**B**) at different lipid concentrations after 24 and 48h of incubation. Data are expressed as mean ± SD (n = 5).

Figure 6. Anti-cancer activity of SLN-Mito versus free Mito on MCF-7 cells at increasing concentrations of Mito (and corresponding lipid concentrations) after 24h (**A**) and 48h (**B**) of incubation. Differences between groups were determined using two-way ANOVA using Tukey's test. Data are expressed as mean ± SD (n = 5). **p<0.01, ***p<0.001, ****p<0.0001.

Figure 7. CLSM z-stacks free drug (**A**) *vs.* SLN-Mito (**B**) at a concentration of 10 μM of Mito in heterotypic spheroids at a penetration depth of 15, 45, 75 and 105 μm, and respective plots of the fluorescence intensity (F. I.) across the spheroid's diameter. Red channel: Mito. Scale bars correspond to 100 μm.

Figure 8. Anti-cancer activity of SLN-Mito versus free Mito on heterotypic spheroids. Data are expressed as mean ± SD (n = 30). Differences between groups were determined using two-way ANOVA using Tukey's test. ***p*<0.01

Figure 9. CLSM images of heterotypic spheroids after incubation with culture medium and free drug and SLN-Mito at a concentration of 21 μM of Mito following Calcein-AM/PI staining. Green channel: Calcein-AM; Red channel: PI. Scale bars correspond to 100 μm.

CRediT authorship contribution statement

Andreia Granja: Conceptualization, Investigation, Data curation, Formal analysis, Writing - original draft. Rita Lima-Sousa: Investigation, Formal analysis, Writing - review & editing. Cátia G. Alves: Investigation, Formal analysis, Writing - review & editing. Duarte de Melo-Diogo: Conceptualization, Supervision, Writing - review & editing. Marina Pinheiro: Supervision, Writing - review & editing. Célia T. Sousa: Supervision, Writing - review & editing. Ilídio J. Correia: Resources, Supervision, Writing - review & editing. Salette Reis: Conceptualization, Resources, Supervision, Writing - review & editing.

Declaration of interests

☒ The authors declare that they have no known competing financial interests or personal relationships that could have appeared to influence the work reported in this paper.

☐ The authors declare the following financial interests/personal relationships which may be considered as potential competing interests:

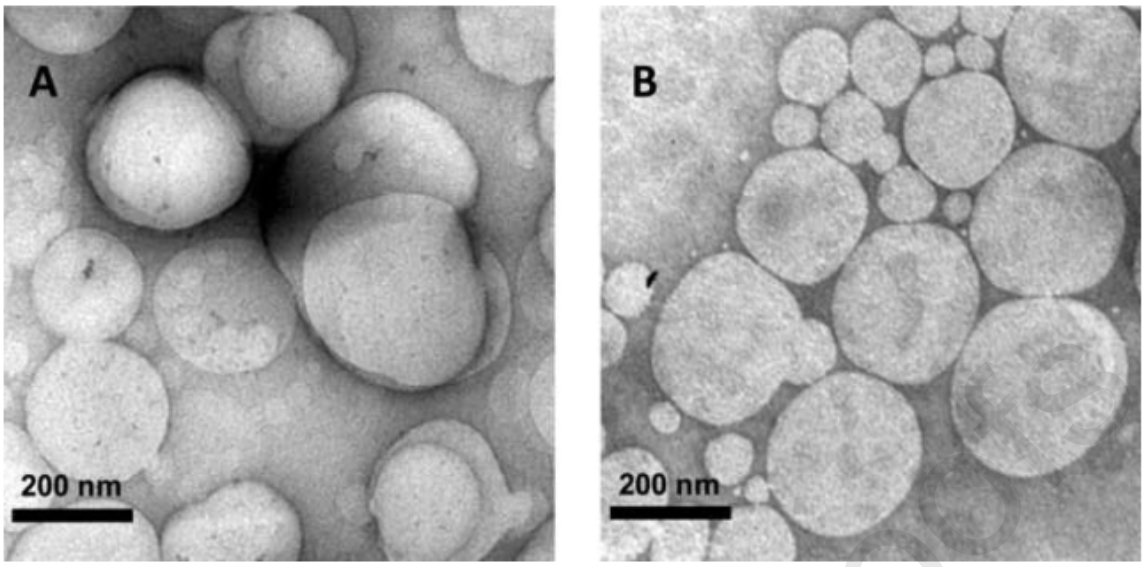

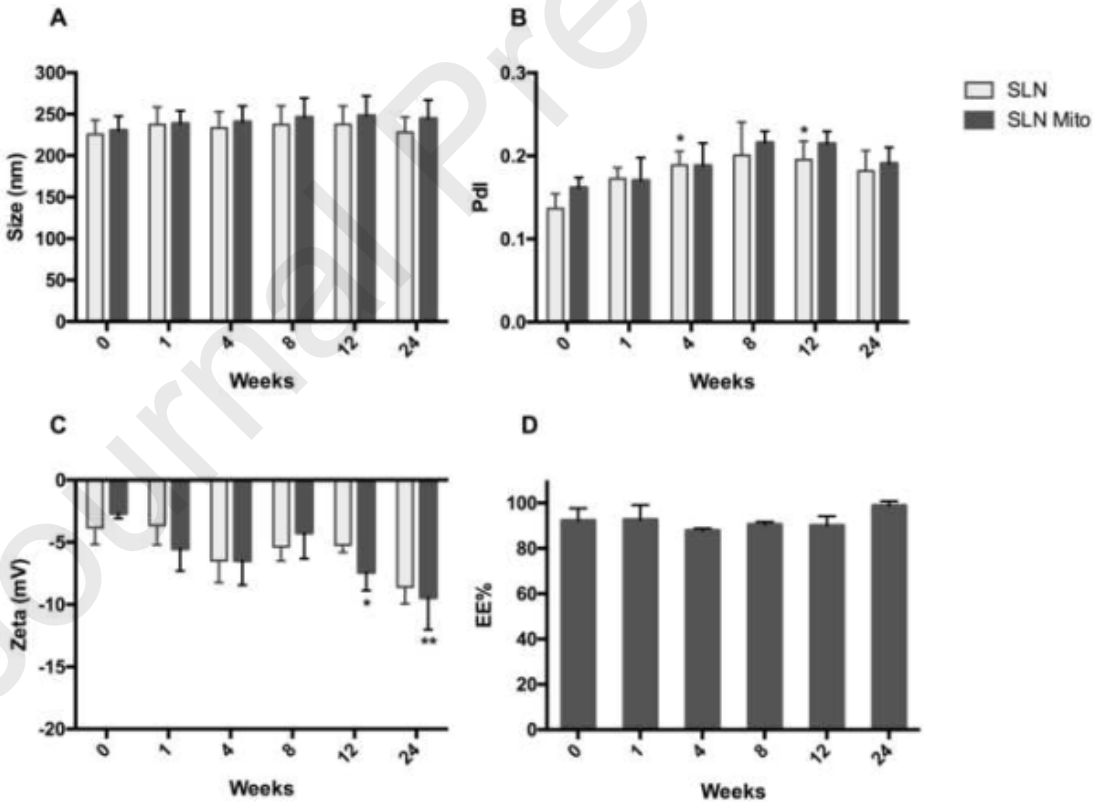

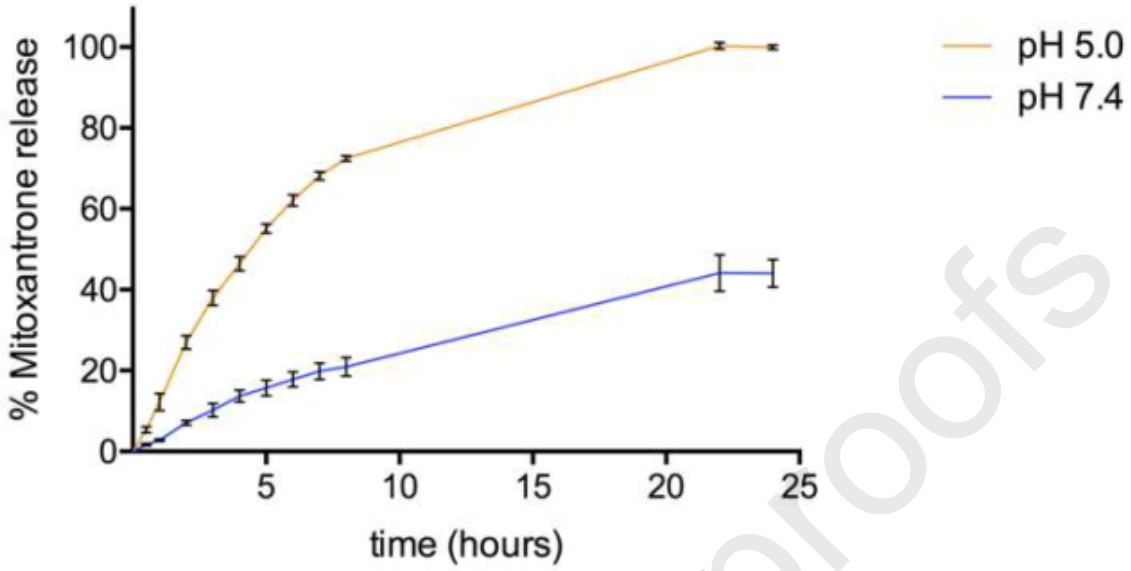

A

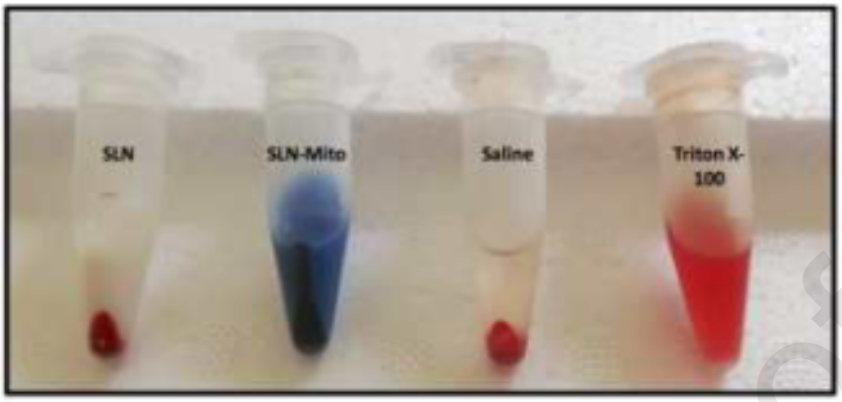

B

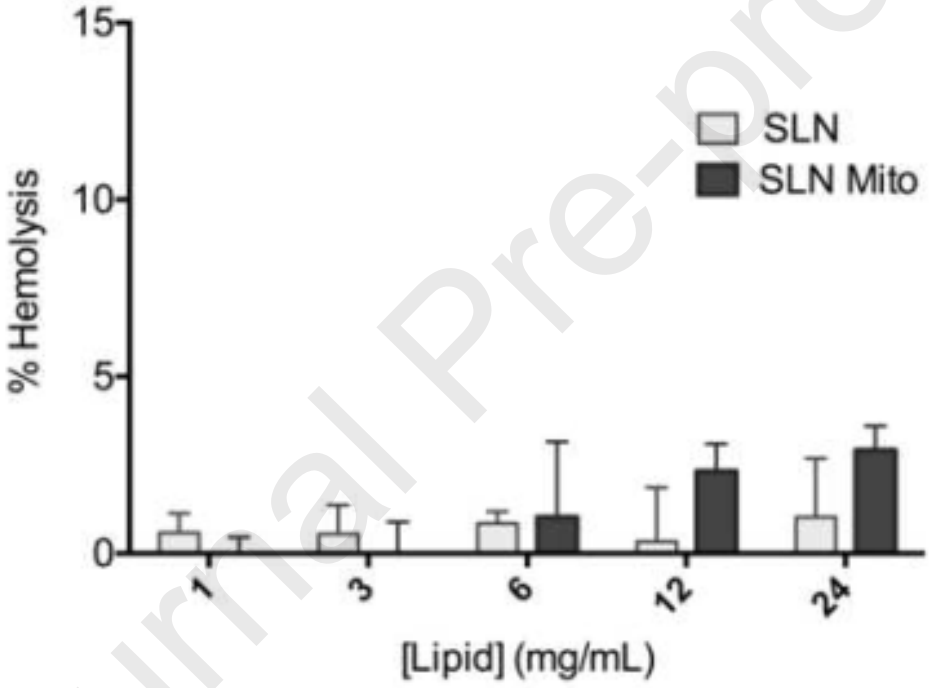

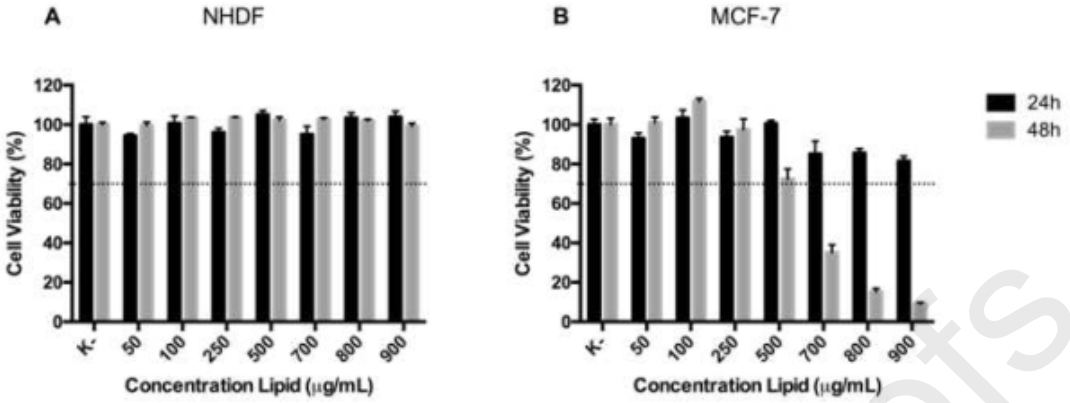

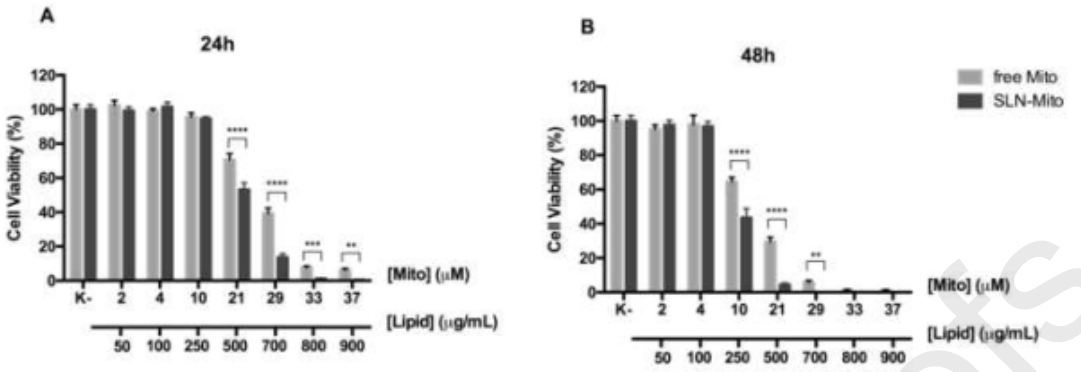

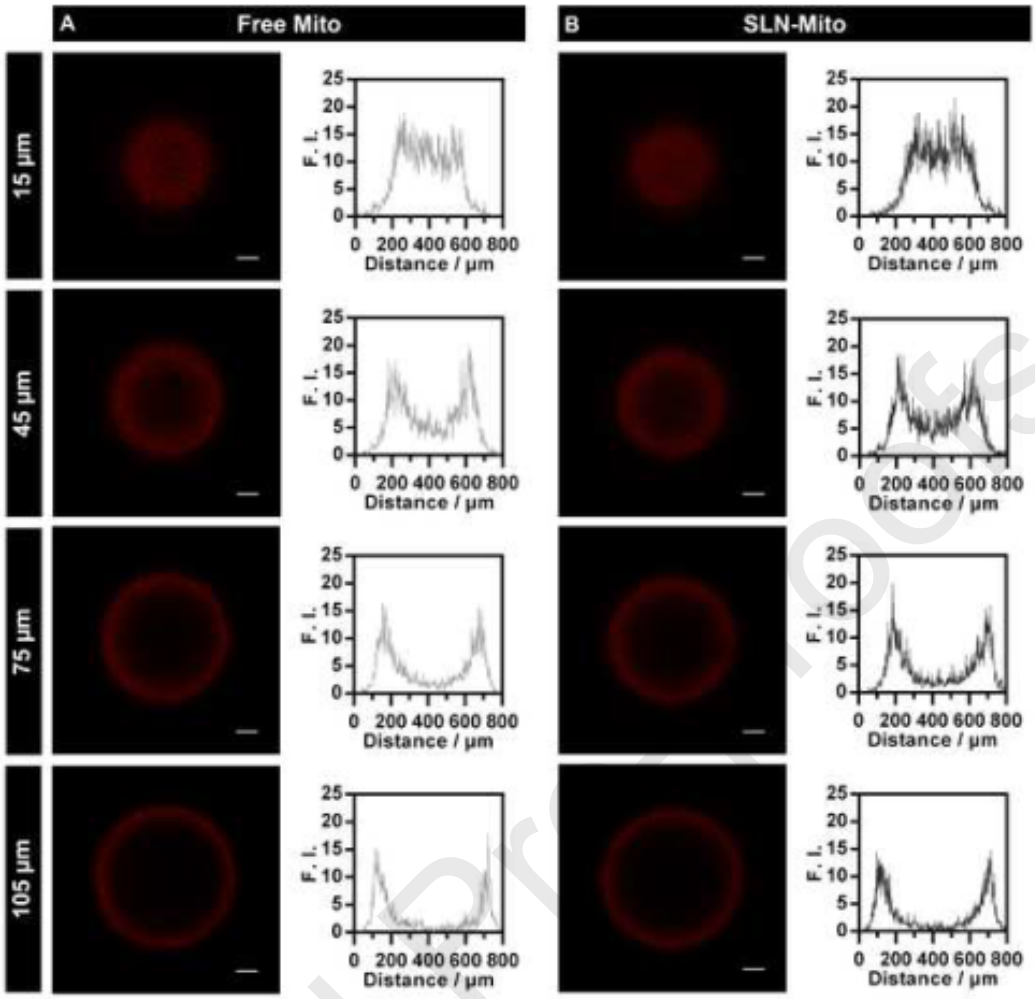

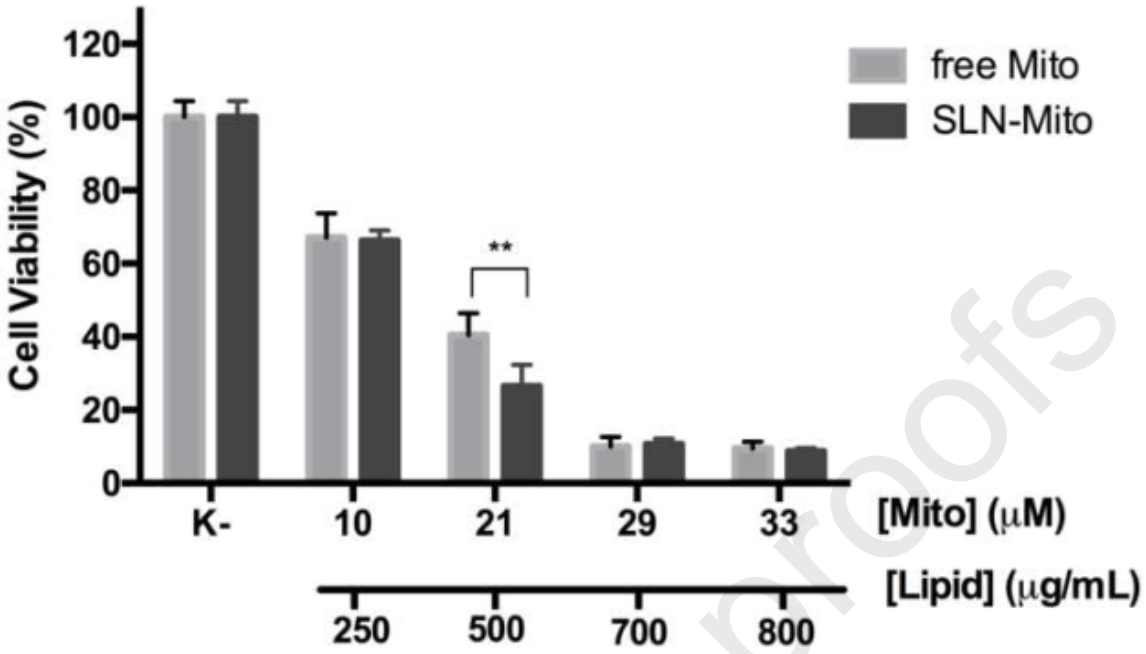

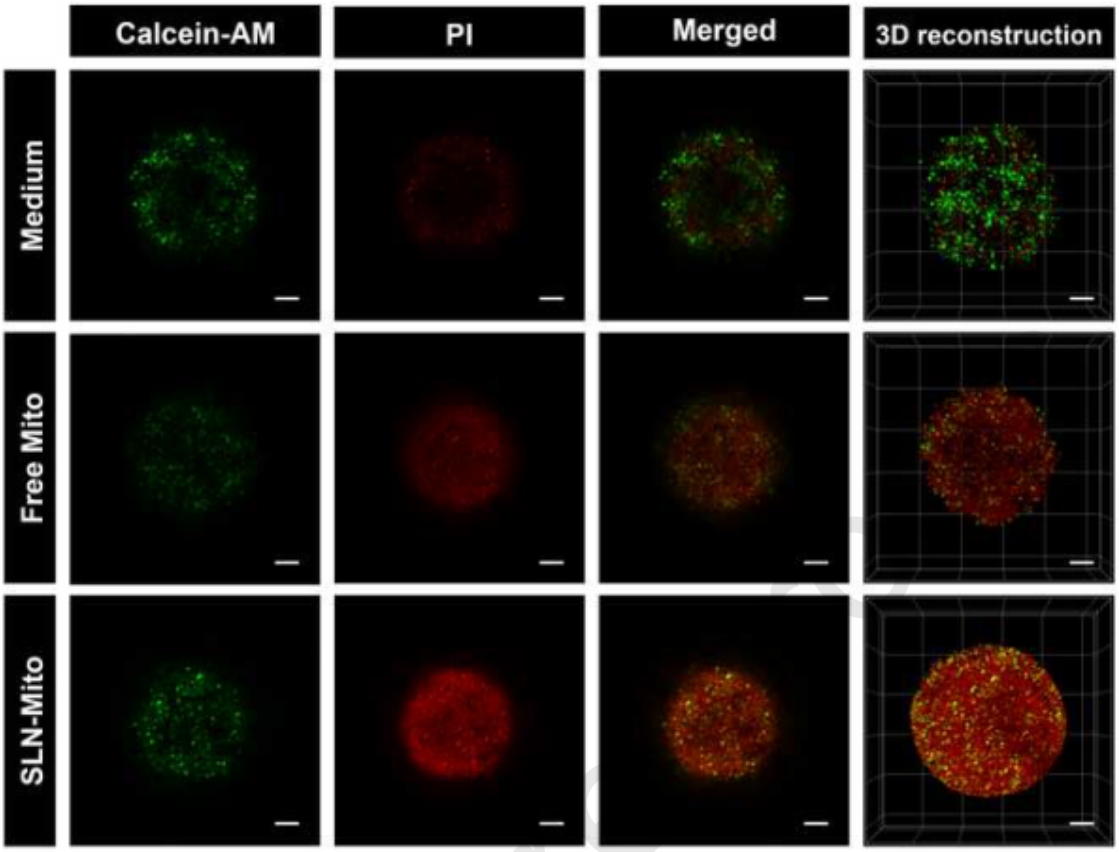

Highlights

- Solid lipid nanoparticles (SLN) were produced using a green, low-cost method
- Nanoparticle production was optimized using a Box-Behnken design
- Nanoparticles were hemo and cytocompatible even at high concentrations of lipid
- The anti-cancer efficacy of the drug was improved in MCF-7 2D models
- SLN could penetrate the tumor spheroids and induce a high anti-tumoral effect